VOL. 28, NO. 8, AUGUST 1990 AIAA JOURNAL

Multigrid Solution of the Navier-Stokes Equations on Triangular Meshes

D. J. Mavriplis*
NASA Langley Research Center, Hampton, Virginia
and
A. Jameson†
Princeton University, Princeton, New Jersey

A new Navier-Stokes algorithm for use on unstructured triangular meshes is presented. Spatial discretization of the governing equations is achieved using a finite-element Galerkin approximation, which can be shown to be equivalent to a finite-volume approximation for regular equilateral triangular meshes. Integration to steady state is performed using a multistage time-stepping scheme, and convergence is accelerated by means of implicit residual smoothing and an unstructured multigrid algorithm. Directional scaling of the artificial dissipation and the implicit residual smoothing operator is achieved for unstructured meshes by considering local mesh stretching vectors at each point. The accuracy of the scheme for highly stretched triangular meshes is validated by comparing computed flat-plate laminar boundary-layer results with the well known similarity solution and by comparing laminar airfoil results with those obtained from various well established structured, quadrilateral-mesh codes. The convergence efficiency of the present method is also shown to be competitive with those demonstrated by structured quadrilateral-mesh algorithms.

I. Introduction

THE use of unstructured triangular meshes in two dimensions and tetrahedral meshes in three dimensions has proven valuable for computing inviscid compressible flow about complex geometries.[1-3] Unstructured meshes also provide a natural setting for the use of adaptive meshing, which has been shown to provide large increases in efficiency and accuracy.[3,4] However, triangular and tetrahedral meshes have seldom been employed for computing viscous flows. Solutions of the full Navier-Stokes equations on triangular meshes can be found in the literature.[3,5-7] However, these are often limited to low-Reynolds-number flows, and/or the accuracy and efficiency of these methods is inferior to that of existing quadrilateral mesh solvers. Consequently, numerous attempts at solving viscous flows for nonsimple configurations have resorted to hybrid structured-unstructured meshing strategies, where structured quadrilateral meshes are employed in the viscous regions, and unstructured meshes are employed in the inviscid regions. Though such strategies have proven valuable for computing flows over various types of configurations,[8] they lack the generality required for arbitrarily complex geometries. The use of completely unstructured meshes in both viscous and inviscid flow regions, as proposed in Ref. 9, holds the promise of producing a more general and flexible method for computing viscous flows over truly arbitrary configurations and provides an ideal setting for the use of adaptive meshing techniques through the viscous layers as well as in regions of strong viscous-inviscid interactions.

For high-Reynolds-number flows over streamlined bodies, viscous effects are confined to thin boundary-layer and wake regions. As the Reynolds number increases, the viscous regions generally become thinner, and the gradients in the normal direction within these regions increase. To accurately resolve such flows, a small mesh spacing is required within the viscous regions. Since the flow gradients are predominantly in the normal direction, it proves economical to refine the mesh only in this direction and to retain a large spacing in the tangential direction. This approach is often employed for quadrilateral meshes and may result in rectangular cells in the viscous regions with aspect ratios up to 10,000:1 for Reynolds numbers of 10×10^6. Clearly, for such cases, refinement in both normal and tangential directions would be prohibitively expensive. Thus, a directional refinement or stretching of the mesh must be employed for triangular meshes as well. This results in highly skewed triangles in the viscous regions, which may potentially degrade the accuracy and efficiency of the scheme.

In this work, a Navier-Stokes solver for unstructured triangular meshes is described. A previously developed unstructured multigrid algorithm[10] is employed to accelerate the convergence of the solution to steady state. Our objective is to demonstrate that by carefully tailoring the scheme for directionally stretched meshes, accurate and efficient solutions can be obtained, which are competitive with those produced by current state-of-the-art, structured, quadrilateral-mesh Navier-Stokes solvers. The solutions presented in this paper consist of laminar flow cases computed on regular stretched triangulations. Although these meshes exhibit an underlying Cartesian structure, as they have been derived from structured quadrilateral meshes, they are treated as completely unstructured data sets by the flow solver. Thus, the solution process does not rely in any way on the regularity of the meshes. It is clear, however, that such meshes may lead to higher solution accuracy than may otherwise be expected with truly irregular unstructured meshes. However, the present effort represents the necessary first step for validating the proposed algorithm and establishing the feasibility of computing viscous flows on highly stretched unstructured meshes which contain a smooth variation of elements through the viscous and inviscid regions. Further investigations will be required to determine the precise

---

Received Feb. 1989; revision received Aug. 1989.

*Staff Scientist, Institute for Computer Applications in Science and Engineering.

†Professor, Department of Mechanical and Aerospace Engineering.

effect of mesh irregularities on the accuracy of the solution in the viscous regions.

II. Discretization of the Governing Equations

In conservative nondimensional form, the full Navier-Stokes equations read

$$\frac{\partial w}{\partial t}+\frac{\partial f_c}{\partial x}+\frac{\partial g_c}{\partial y}=\frac{\sqrt{\gamma}M_\infty}{Re_\infty}\left(\frac{\partial f_v}{\partial x}+\frac{\partial g_v}{\partial y}\right) \tag{1}$$

where w is the solution vector and f_c and g_c are the Cartesian components of the convective fluxes

$$w=\begin{bmatrix}\rho\\ \rho u\\ \rho v\\ \rho E\end{bmatrix}\quad f_c=\begin{bmatrix}\rho u\\ \rho u^2+p\\ \rho uv\\ \rho uE+up\end{bmatrix}\quad g_c=\begin{bmatrix}\rho v\\ \rho vu\\ \rho v^2+p\\ \rho vE+vp\end{bmatrix} \tag{2}$$

In the above equation, ρ represents the fluid density, u and v the x and y components of fluid velocity, E the total energy, and p is the pressure which can be calculated from the equation of state of a perfect gas

$$p=(\gamma-1)\rho\left(E-\frac{(u^2+v^2)}{2}\right) \tag{3}$$

The viscous fluxes f_v and g_v are given by

$$f_v=\begin{bmatrix}0\\ \sigma_{xx}\\ \sigma_{xy}\\ u\sigma_{xx}+v\sigma_{xy}-q_x\end{bmatrix}\quad g_v=\begin{bmatrix}0\\ \sigma_{xy}\\ \sigma_{yy}\\ u\sigma_{xy}+\sigma_{yy}-q_y\end{bmatrix} \tag{4}$$

where σ represents the stress tensor and q the heat flux vector, which are given by the constitutive equations for a Newtonian fluid

$$\begin{aligned}
\sigma_{xx}&=2\mu u_x-\tfrac{2}{3}\mu(u_x+v_y)\\
\sigma_{yy}&=2\mu v_y-\tfrac{2}{3}\mu(u_x+v_y)\\
\sigma_{xy}&=\sigma_{yx}=\mu(u_y+v_x)\\
q_x&=-k\frac{\partial T}{\partial x}=-\frac{\gamma}{\gamma-1}\frac{\mu}{Pr}\frac{\partial(p/\rho)}{\partial x}\\
q_y&=-k\frac{\partial T}{\partial y}=-\frac{\gamma}{\gamma-1}\frac{\mu}{Pr}\frac{\partial(p/\rho)}{\partial y}
\end{aligned} \tag{5}$$

γ is the ratio of specific heats of the fluid, M_∞ the freestream Mach number, Re_∞ the Reynolds number based on the airfoil chord, and Pr the Prandtl number. The coefficient of viscosity μ varies with the temperature of the fluid and is calculated as

$$\mu=KT^{0.72} \tag{6}$$

where K is a constant. Since μ and T are both nondimensionalized with respect to their freestream values, the constant K can be set equal to 1. Equation (1) represents a set of partial differential equations, which must be discretized in space in order to obtain a set of coupled ordinary differential equations, which can be then be integrated in time to obtain the steady-state solution.

The spatial discretization procedure begins by storing flow variables at the vertices of the triangles. The stress tensor σ and the heat flux vector q must be calculated at the centers of the triangles. This is achieved by computing the required first differences in the flow variables [(from Eqs. (5)] at the triangle centers. For a piecewise linear approximation of the flow variables in space, the first differences are constant over each triangle and may be computed as

$$\begin{aligned}
w_x&=\frac{1}{A}\iint\frac{\partial w}{\partial x}\,\mathrm{d}x\mathrm{d}y=\frac{1}{A}\oint w\,\mathrm{d}y\\
&=\frac{1}{A}\sum_{k=1}^{3}\frac{w_{k+1}+w_k}{2}(y_{k+1}-y_k)
\end{aligned} \tag{7}$$

$$\begin{aligned}
w_y&=\frac{1}{A}\iint\frac{\partial w}{\partial y}\,\mathrm{d}x\mathrm{d}y=-\frac{1}{A}\oint w\,\mathrm{d}x\\
&=-\frac{1}{A}\sum_{k=1}^{3}\frac{w_{k+1}+w_k}{2}(x_{k+1}-x_k)
\end{aligned} \tag{8}$$

where the summation over k refers to the three vertices of the triangle and is cyclic such that $w_4=w_1$ and $y_4=y_1$. The flux balance equations are obtained by a Galerkin finite-element-type formulation. The Navier-Stokes equations are first rewritten in vector notation

$$\frac{\partial w}{\partial t}+\nabla\cdot\boldsymbol{F}_c=\frac{\sqrt{\gamma}M_\infty}{Re_\infty}\nabla\cdot\boldsymbol{F}_v \tag{9}$$

The F_c is a dyadic (second-order tensor), the Cartesian components of which are given by the f_c and g_c convective flux vectors defined in Eq. (4). Similarly, f_v and g_v represent the Cartesian components of the viscous flux dyadic F_v. Multiplying by a test function ϕ, and integrating over physical space yields

$$\frac{\partial}{\partial t}\iint_\Omega\phi w\,\mathrm{d}x\mathrm{d}y+\iint_\Omega\phi\nabla\cdot\boldsymbol{F}_c\,\mathrm{d}x\mathrm{d}y=\frac{\sqrt{\gamma}M_\infty}{Re_\infty}\times\iint_\Omega\phi\nabla\cdot\boldsymbol{F}_v\,\mathrm{d}x\mathrm{d}y \tag{10}$$

Integrating the flux integrals by parts and neglecting boundary terms gives

$$\frac{\partial}{\partial t}\iint_\Omega\phi w\,\mathrm{d}x\mathrm{d}y=\iint_\Omega\boldsymbol{F}_c\cdot\nabla\phi\,\mathrm{d}x\mathrm{d}y-\frac{\sqrt{\gamma}M_\infty}{Re_\infty}\times\iint_\Omega\boldsymbol{F}_v\cdot\nabla\phi\,\mathrm{d}x\mathrm{d}y \tag{11}$$

In order to evaluate the flux balance at a vertex P, ϕ is taken as a piecewise linear function which has the value 1 at node P and vanishes at all other vertices. Therefore, the integrals in the above equation are nonzero only over triangles which contain the vertex P and thus define the domain of influence of node P as shown in Fig. 1. To evaluate the above integrals, we make use of the fact that ϕ_x and ϕ_y are constant over a triangle and may be evaluated as per Eqs. (7) and (8). The

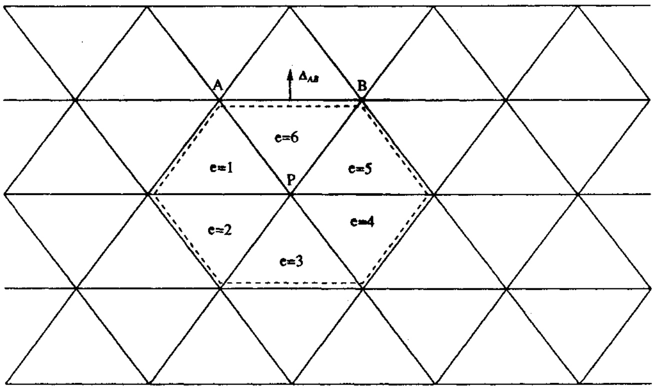

Fig. 1 Domain of influence of node P and equivalent control volume for a finite-volume approximation to the convective terms.

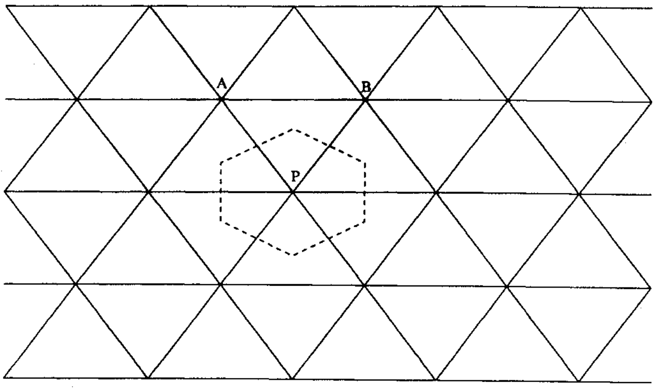

Fig. 2 Equivalent control volume for a finite-volume approximation to the viscous terms.

convective fluxes F_c are taken as piecewise linear functions in space, and the viscous fluxes F_v are piecewise constant over each triangle since they are formed from first derivatives in the flow variables. Evaluating the flux integrals with these assumptions, one obtains

$$\frac{\partial}{\partial t}\iint_{\Omega} \phi w \, \mathrm{d}x\mathrm{d}y = \sum_{e=1}^{n} \frac{F_c^A + F_c^B}{6} \cdot \Delta L_{AB}$$

$$- \frac{\sqrt{\gamma} M_\infty}{Re_\infty} \sum_{e=1}^{n} \frac{F_v^e}{2} \cdot \Delta L_{AB} \tag{12}$$

where the summations are over all triangles in the domain of influence as shown in Fig. 1. The Δ_{AB} represents the directed (normal) edge length of the face of each triangle on the outer boundary of the domain; F_c^A and F_c^B are the convective fluxes at the two vertices at either end of this edge, and F_v^e is the viscous flux in triangle e. If the integral on the left side of Eq. (12) is evaluated in the same manner, the time derivatives become coupled in space. Since we are not interested in the time accuracy of the scheme, but only in the final steady-state solution, we employ the concept of a lumped mass matrix. This is equivalent to assuming w to be constant over the domain of influence while integrating the left side. Hence, we obtain

$$\Omega_p \frac{\partial w_p}{\partial t} = \sum_{e=1}^{n} \frac{F_c^A + F_c^B}{2} \cdot \Delta L_{AB} - \frac{\sqrt{\gamma} M_\infty}{Re_\infty} \sum_{e=1}^{n} \frac{3}{2} (F_v^e \cdot \Delta L_{AB}) \tag{13}$$

where the factor of ⅓ is introduced by the integration of ϕ over the domain, and Ω_p represents the surface area of the domain of influence of P. For the convective fluxes, this procedure is equivalent to the vertex finite-volume formulation described in Refs. 1 and 10. For the viscous fluxes, in the case of equilateral triangles, this formulation can be shown to be equivalent to a finite-volume formulation where the control volume is taken as the hexagonal cell formed by joining the centroids of all triangles with a vertex at P as shown in Fig. 2. For a smoothly varying regular triangulation, the above formulation is second-order accurate.

III. Artificial Dissipation

In principle, the physical viscous terms of the Navier-Stokes equations are capable of providing the numerical scheme with the dissipative property necessary for stability and capturing discontinuities. However, for high-Reynolds-number flows, this can only be achieved by resorting to extremely small mesh spacings throughout the domain. Thus, in practice, it is necessary to introduce artificial dissipative terms to maintain stability in the essentially inviscid portions of the flowfield and to efficiently capture discontinuities. These additional dissipative terms must be carefully constructed to ensure that the accuracy of the scheme is preserved both in the inviscid region of the flowfield where the convective terms dominate as well as in the boundary-layer and wake regions where the artificial dissipation terms must be much smaller than the physical viscous terms. Previous Navier-Stokes solutions on highly stretched structured meshes[11-13] have demonstrated the need for different scalings of the artificial dissipation terms in the streamwise and normal directions within the regions of viscous flow. However, for unstructured meshes, directional scaling is significantly more difficult to achieve since no mesh coordinate lines exist. In fact, unstructured meshes have traditionally been considered to be truly multidimensional, isotropic constructions with no preferred directions. However, as stated previously, the efficient solution of high-Reynolds-number viscous flows requires the use of meshes with highly stretched elements in the boundary-layer and wake regions since these physical phenomena are highly directional in nature. For such meshes, even in the unstructured case, a direction and magnitude of stretching can be defined for each mesh point, as shown in Fig. 3. This stretching vector, denoted as s, need not necessarily line up with any of the mesh edges. For the meshes employed in this paper, which are directly derived from structured quadrilateral meshes by splitting each quadrilateral into two triangles, the stretching magnitude and direction may be taken as the aspect ratio and the major axis of the generating quadrilateral element for each triangular element, respectively. In the more general case, the generation of directionally stretched unstructured meshes[9,14] requires the definition of local stretching vectors thoughout the flowfield. These can in turn be used to scale the dissipation terms. It is important to note that these stretching vectors represent grid metrics which do not depend on the flow solution.

The artificial dissipation operator on unstretched, unstructured meshes has previously been constructed as a blend of undivided Laplacian and biharmonic operators in the flowfield. Since the biharmonic operator may be viewed as a Laplacian of a Laplacian, the dissipation operator may be reformulated as a global undivided Laplacian operating on a blend of the flow variables and their second differences:

$$D(w) = \Omega\alpha[u_{xx} + u_{yy}] \tag{14}$$

where

$$u = \kappa'_2 w - \kappa_4 \nabla^2 w \tag{15}$$

In the above equations, Ω represents the area of the control volume, which is of order Δx^2, and $\nabla^2 w$ denotes the undivided Laplacian of w. The first term in the above equation constitutes a relatively strong first-order dissipation term, which is necessary to prevent unphysical oscillations in the vicinity of a shock. To preserve the second-order accuracy of the scheme, this term must be turned off in regions of smooth

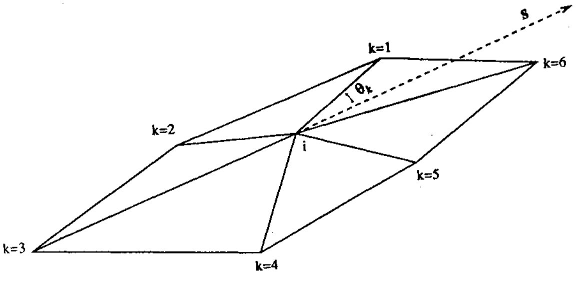

Fig. 3 Definition of a local stretching vector for unstructured triangular meshes and coordinate system associated with stretching direction.

flow. This is accomplished by evaluating κ_2' at mesh point i as

$$(\kappa_2')_i = \kappa_2 \frac{\sum_{k=1}^{n} [p_k - p_i]}{\sum_{k=1}^{n} [p_k + p_i]} \tag{16}$$

Hence κ_2' is proportional to an undivided Laplacian of the pressure, which is constructed as a summation of the pressure differences along all edges meeting at node i, as depicted in Fig. 3. This construction has the required property of being of order unity near a shock and small elsewhere. The κ_2 is an empirically determined coefficient which is taken as 0 for subcritical flows and as 1/2 for transonic and supersonic flows. In Eq. (14), the overall scaling of the dissipation is performed by the factor α, which has previously been taken as proportional to the maximum eigenvalue of the Euler equations for inviscid flow calculations.[4] Directional scaling of the dissipation may thus be achieved by replacing Eq. (14) by

$$D(w) = \Omega[\alpha_1 u_{\xi\xi} + \alpha_2 u_{\eta\eta}] \tag{17}$$

where α_1 and α_2 represent the different scalings in the ξ and η directions, respectively. Here, ξ denotes the direction of the mesh stretching and η the direction normal to ξ. Appropriate expressions for α_1 and α_2 remain to be determined as well as the discretization procedure for the above operator on unstructured meshes.

On structured meshes, the dissipation is often scaled by the maximum eigenvalue of the Euler equations in each mesh coordinate direction, which is given by

$$\lambda_\xi = [\,|u| + c]\,\Delta\eta \qquad \lambda_\eta = [\,|v| + c]\,\Delta\xi \tag{18}$$

where u, v, and $\Delta\xi$, $\Delta\eta$ represent the local fluid velocity components and the mesh spacings in the two mesh coordinate directions, and c denotes the local speed of sound. However, for efficient multigrid convergence, a more even distribution of the dissipation is required in the two mesh coordinate directions, and the above scaling is replaced by[11,13]

$$\bar{\lambda}_\xi = \phi(r)\lambda_\xi \qquad \bar{\lambda}_\eta = \phi(r^{-1})\lambda_\eta \tag{19}$$

where

$$\phi(r) = 1 + r^{2/3} \tag{20}$$

and

$$r = \frac{\lambda_\eta}{\lambda_\xi} = \frac{[\,|v| + c]\,\Delta\xi}{[\,|u| + c]\,\Delta\eta} \tag{21}$$

On unstructured meshes, we begin by constructing an isotropic value of the maximum eigenvalue at each mesh point as

$$\lambda = \int_{\partial\Omega} |u\,x\,\mathrm{d}\ell| + c\,|\mathrm{d}\ell| \tag{22}$$

where the integration is performed around the boundary of the control volume for the particular mesh point being considered. The discrete approximation to the above integral yields the final form for λ

$$\lambda = \sum_{e=1}^{n} |u_{AB}\Delta y_{AB} - v_{AB}\Delta x_{AB}| + c_{AB}\sqrt{\Delta x^2_{AB} + \Delta y^2_{AB}} \tag{23}$$

where Δx_{AB} and Δy_{AB} represent the x and y increments along the outer edge AB of element e, as shown in Fig. 1, and u_{AB}, v_{AB}, and c_{AB} represent averaged values along the edge AB. By considering the equivalent integration around the control volume on a structured quadrilateral mesh, it can be seen that λ approximates the sum of the eigenvalues in the two space dimensions, i.e.,

$$\lambda \approx \lambda_\xi + \lambda_\eta \tag{24}$$

Furthermore, the magnitude of the stretching vector s on the unstructured mesh can be considered to be closely related to the cell aspect ratio. Thus, by analogy with the structured mesh case

$$s \approx \frac{\Delta\xi}{\Delta\eta} \approx \frac{\lambda_\eta}{\lambda_\xi} \tag{25}$$

where s represents the magnitude of s, and the second approximation assumes that the magnitude of the speed of sound c is much greater than the streamwise and normal velocities u and v in the viscous flow regions. Thus, Eqs. (24) and (25) permit an estimate of the values of the maximum eigenvalues in the directions parallel and normal to the local mesh stretching vector, given the values of λ and s. From Eqs. (19-21), the α_1 and α_2 coefficients of Eq. (17) are constructed as

$$\alpha_1 = \phi(s)\frac{1}{s+1}\lambda \qquad \alpha_2 = \phi(s^{-1})\frac{s}{s+1}\lambda \tag{26}$$

Next, the discretization of the scaled Laplacian of Eq. (17) on unstructured meshes must be considered. Previously, for inviscid flows,[1,4] the unscaled Laplacian of Eq. (14) was approximated as an accumulated edge difference in computational space, i.e.,

$$u_{xx} + u_{yy} = \frac{1}{\Omega}\sum_{k=1}^{n} [u_k - u_i] \tag{27}$$

where $k = 1,\ldots,n$ represents the n neighbors of node i, and the difference is taken along all edges meeting at node i. For a Cartesian grid, this reduces to the familiar five-point Laplacian finite-difference formula. Equation (17) can easily be approximated on a Cartesian mesh aligned with the ξ and η coordinate directions, simply by multiplying the constructed second differences in the ξ and η directions by α_1 and α_2, respectively. Alternatively, this can be obtained by considering the finite-volume approximation to a Laplacian on a Cartesian mesh in a stretched computational space, where $\sqrt{\alpha_1}$ stretching is applied in the ξ direction, and $\sqrt{\alpha_2}$ stretching is applied in the η direction. By considering the equivalent stretching of computational space for unstructured meshes, a finite-volume approximation to the Laplacian yields the discretization formula for the directionally scaled dissipation operator[15]

$$\begin{aligned} D(w_i) = \Omega\,[\alpha_1 u_{\xi\xi} + \alpha_2 u_{\eta\eta}] = \sum_{k=1}^{n} [u_k - u_i] \\ \times [\alpha_1 \cos^2\theta_k + \alpha_2 \sin^2\theta_k] \end{aligned} \tag{28}$$

where θ_k represents the angle between the kth mesh edge at node i, and the principal stretching direction ξ, as shown in Fig. 3. From the above equation, it can be seen that if the kth mesh edge coincides with the ξ or η directions, then the difference along that edge is multiplied by α_1 or α_2, respectively, and if $\alpha_1 = \alpha_2$, then the above discretization reduces to the isotropic accumulated edge difference previously employed. Since in practice α_1 and α_2 vary throughout the mesh, Eq. (28) is replaced by

$$D(w_i) = \sum_{k=1}^{n} [u_k - u_i] = \left[\frac{A_k + A_i}{2}\right] \tag{29}$$

where

$$A_k = \alpha_{1k}\cos^2\theta_k + \alpha_{2k}\sin^2\theta_k \tag{30}$$

and the i and k subscripts refer to variables evaluated at nodes i and k, thus ensuring a conservative formulation of the dissipation operator.

IV. Integration to Steady State

The discretization of the spatial derivatives transforms Eq. (1) into the set of coupled ordinary differential equations

$$\Omega_i \frac{\mathrm{d}w_i}{\mathrm{d}t} + [Q(w_i) - D(w_i)] = 0, \qquad i = 1,2,3,\ldots,n \tag{31}$$

where n is the number of mesh nodes. The residual $Q(w)$ represents the discrete approximation to the convective fluxes. The $D(w)$ now represents the dissipative terms, i.e., the discrete approximation to the viscous fluxes, as well as the artificial dissipation terms. These equations are integrated in time using a five-stage, hybrid, time-stepping scheme given by

$$\begin{aligned}
w^{(0)} &= w^{n}\\
w^{(1)} &= w^{(0)} - \alpha_1 \frac{\Delta t}{\Omega}\left[Q(w^{(0)}) - D_0\right]\\
w^{(2)} &= w^{(0)} - \alpha_2 \frac{\Delta t}{\Omega}\left[Q(w^{(1)}) - D_1\right]\\
w^{(3)} &= w^{(0)} - \alpha_3 \frac{\Delta t}{\Omega}\left[Q(w^{(2)}) - D_2\right]\\
w^{(4)} &= w^{(0)} - \alpha_4 \frac{\Delta t}{\Omega}\left[Q(w^{(3)}) - D_3\right]\\
w^{(5)} &= w^{(0)} - \alpha_5 \frac{\Delta t}{\Omega}\left[Q(w^{(4)}) - D_4\right]\\
w^{n+1} &= w^{(5)}
\end{aligned} \tag{32}$$

where

$$D_0 = D_1 = D(w^{(0)})$$

$$D_2 = D_3 = \beta D(w^{(2)}) + (1-\beta)\, D_0$$

$$D_4 = \gamma D(w^{(4)}) + (1-\gamma)\, D_2$$

w^n represents the value of the solution vector at the nth time step, and $w^{(q)}$ represents the value at the qth stage within a time step. The dissipative operator $D(w)$ is evaluated only at the first, third, and fifth stages of the scheme and is employed to construct the subscripted D_q operator, which represents a linear combination of present and previous evaluations of $D(w)$. This scheme represents a particular case of a large class of multistage, time-stepping schemes where the coefficients are chosen in order to maintain good stability properties when the viscous terms are dominant and to ensure large damping of high-frequency errors, which is crucial for a rapidly convergent multigrid method.[11] The values of these coefficients are taken as

$$\beta = 0.56 \qquad \gamma = 0.44$$

and

$$\alpha_1 = 1/4 \quad \alpha_2 = 1/6 \quad \alpha_3 = 3/8 \quad \alpha_4 = 1/2 \quad \alpha_5 = 1$$

A. Local Time Stepping

Convergence to the steady-state solution may be accelerated by sacrificing the time accuracy of the scheme and advancing the equations at each mesh point in time by the maximum permissible time step in that region, as determined by local stability analysis. Stability limitations due to both the convective and diffusive characters of the Navier-Stokes equations must be considered. The local time step is thus taken as

$$\Delta t = CFL \left(\frac{\Delta t_c \Delta t_v}{\Delta t_c + \Delta t_v}\right) \tag{33}$$

where CFL is the Courant number for the particular time-stepping scheme, and Δt_c and Δt_v represent the individual convective and viscous time-step limits, respectively. The convective time-step limit has previously been derived for Euler solutions on unstructured meshes[4] and is given by

$$\Delta t_c = \frac{\Omega}{\lambda_c} \tag{34}$$

where λ_c, previously denoted simply as λ, represents the maximum eigenvalue of the inviscid equations averaged around the boundary of the control volume as given in Eq. (23), and Ω denotes the area of the control volume. The viscous time-step limit is taken as

$$\Delta t_v = K_v \frac{\Omega}{\lambda_v} \tag{35}$$

where K_v is an empirically determined coefficient which determines the relative importance of the viscous and inviscid time-step limits in the final expression and has been taken as 0.25 in this work. The λ_v represents the maximum eigenvalue of the diffusive operator of the Navier-Stokes equations, averaged about the boundary of the control volume. For the structured mesh case, $\lambda_{v\xi}$ and $\lambda_{v\eta}$ in the two mesh coordinate directions have been derived in Ref. 11. For example,

$$\lambda_{v\xi} = \frac{\sqrt{\gamma} M_\infty}{Re\Omega}\left[\frac{\gamma\mu}{Pr\rho}\Delta\eta^2 + \frac{\mu}{3\rho}\Delta\xi\Delta\eta\right] \tag{36}$$

with a similar expression for $\lambda_{v\eta}$. If the cross terms are neglected, λ_v for unstructured meshes may thus be approximated as

$$\lambda_v = \frac{\sqrt{\gamma} M_\infty}{Re\Omega} \int_{\partial\Omega} \frac{\gamma\mu}{Pr\rho}\, \mathrm{d}l^2 \tag{37}$$

where the integration is performed along the boundary of the control volume. In discrete form, the expression for λ_v becomes

$$\lambda_v = \frac{\gamma^{3/2} M_\infty}{Re\ Pr\ \Omega} \sum_{e=1}^{n} \frac{\mu_{AB}}{\rho_{AB}} \left|\Delta x^2{}_{AB} + \Delta y^2{}_{AB}\right| \tag{38}$$

where μ_{AB} and ρ_{AB} represent averaged values of viscosity and density along the outer edge AB of each element e (see Fig. 1).

B. Implicit Residual Smoothing

The stability range of the basic time-stepping scheme can be increased by implicitly smoothing the residuals. Thus the original residuals R may be replaced by the smoothed residuals $\bar{R}$ by solving the implicit equations

$$\bar{R}_i = R_i + \epsilon \nabla^2 \bar{R}_i \tag{39}$$

at each mesh point i, where $\nabla^2 \bar{R}_i$ represents the undivided Laplacian of the residuals, and ϵ is the smoothing coefficient. For highly stretched structured meshes, the use of individual smoothing coefficients in the ξ and η mesh coordinate directions, which vary locally throughout the mesh, has been found to result in significantly improved convergence rates.[11,13] The use of locally varying smoothing coefficients has the effect of making the scheme more implicit in the direction normal to the boundary layer, or normal to the mesh stretching direction, and less implicit in the tangential direction. The implementation of implicit residual smoothing with locally varying coefficients on unstructured meshes is accomplished by rewriting Eq. (39) as

$$\bar{R}_i = R_i + \epsilon_\xi \bar{R}_{i_{\xi\xi}} + \epsilon_\eta \bar{R}_{i_{\eta\eta}} \tag{40}$$

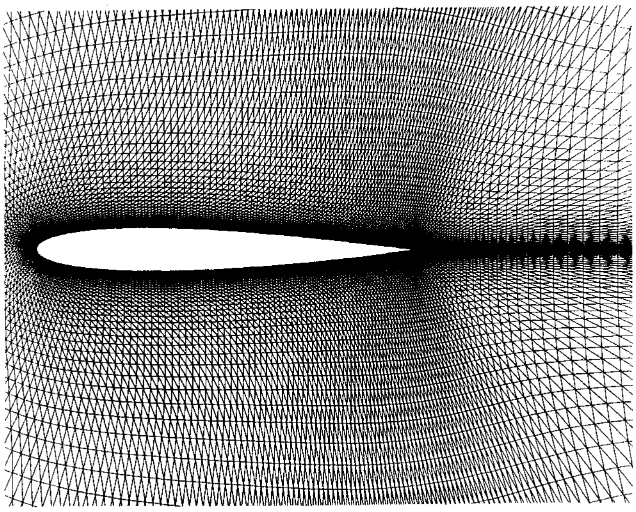

Fig. 4 Stretched triangular mesh about a NACA 0012 airfoil employed for the low-Reynolds number calculations; number of nodes = 20,800, number of triangles = 41,600.

where ξ and η now represent the directions tangential and normal to the local mesh stretching vector, as described previously. By analogy with the structured mesh case of Ref. 11 and making use of Eq. (25), the smoothing coefficients are taken as

$$\epsilon_\xi = \max\left[\frac{1}{4}\left[\left(\frac{CFL}{CFL^*}\frac{1}{s+1}\phi(s)\right)^2 - 1\right], 0\right] \tag{41}$$

$$\epsilon_\eta = \max\left[\frac{1}{4}\left[\left(\frac{CFL}{CFL^*}\frac{s}{s+1}\phi(s^{-1})\right)^2 - 1\right], 0\right] \tag{42}$$

where CFL and CFL^* are the Courant numbers of the smoothed and unsmoothed schemes, respectively, s denotes the magnitude of the mesh stretching vector, and ϕ is given by Eq. (20). Since Eq. (40) now contains a directionally scaled Laplacian, it can be discretized on an unstructured mesh in a manner analogous to that employed for the directionally scaled dissipation operator as given in Eq. (28). For economy, the resulting set of algebraic equations are solved only approximately by performing two Jacobi iterations.

C. Multigrid Algorithm

The idea of a multigrid algorithm is to accelerate the convergence of the fine mesh solution by efficiently damping out the low-frequency error components by means of time stepping on coarser meshes. A multigrid method for unstructured meshes has previously been developed for inviscid flow calcutations.[10] It assumes the various coarse and fine meshes of the sequence to be completely independent from one another and computes the patterns for transferring the flow variables, corrections, and residuals back and forth between the various meshes in a preprocessing operation where an efficient tree-search algorithm is employed. For viscous flow calculations, a full multigrid (FMG) algorithm is employed where the initial flowfield on the fine grid is obtained by interpolating a flow solution, which has been converged on the previous coarser grid with a small number (10–20) of multigrid cycles. Better convergence and additional robustness can also be obtained if the previously employed V cycle is replaced by a W cycle, which performs one time step on each mesh when proceeding from fine to coarse meshes and no time stepping but merely prolongation of the corrections when proceeding from coarse grids to fine grids. It also proves useful to implicitly smooth the corrections after the prolongation operation when proceeding from coarse to fine meshes. The constant coefficient implicit smoothing operator of Eq. (39) is employed for this operation using a value of $\epsilon = 0.2$, and the resulting equations are solved approximately using two Jacobi iterations.

V. Results

The intent of this work is to provide a validation of the basic algorithm described above for triangular meshes and to demonstrate that accurate and efficient solutions can be obtained on triangular meshes with highly stretched elements. This is best accomplished by computing solutions with the present scheme on triangular meshes, which are directly derived from structured quadrilateral meshes, and comparing the accuracy and efficiency of these solutions with those obtained on equivalent quadrilateral meshes with proven structured-mesh Navier-Stokes solvers.[11–13] Although the triangular meshes exhibit an underlying structure, they are treated as an unstructured data set by the flow solver. The mesh stretching vectors, which are used to scale the artificial dissipation and residual smoothing operators, are directly derived from the underlying structured mesh. This, however, does not represent an essential limitation of the present scheme since it has been shown how mesh stretching vectors can be defined and employed in the mesh generation phase for arbitrary unstructured meshes.[9,14]

A. Low Reynolds Number Cases

The first series of test cases involve very low Reynolds number flows over a NACA0012 airfoil, which have been computed by various authors for the GAMM workshop on the Solution of Compressible Navier-Stokes Flows.[16] For these cases, the thin-layer assumption does not hold, and the flow is dominated by viscous effects, thus, providing a means of validating the discretization of the full Navier-Stokes viscous terms implemented in this work. The mesh employed for these calculations is depicted in Fig. 4. It contains 20,800 points and 41,600 triangles and is derived from a 320 × 64 structured quadrilateral C mesh with 192 points on the airfoil, and 64 points in the wake. The far-field boundary is located 15 chords out from the airfoil, and the mesh spacing in the normal direction at the wall is 0.002 chords resulting in relatively lowcell aspect ratios of the order of 10:1 on the airfoil surface and 100:1 in the wake region. For all these cases, a constant temperature wall boundary condition is prescribed along the airfoil surface where the temperature is taken as the adiabatic freestream temperature.

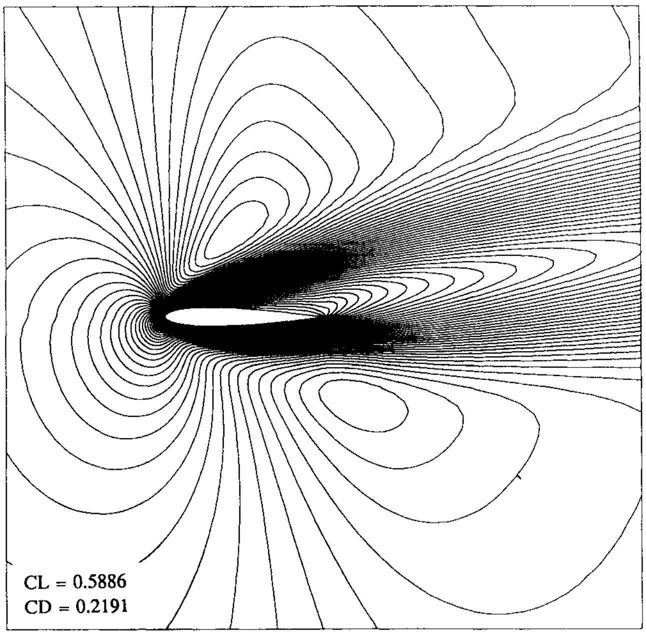

Fig. 5 Mach number contours of computed solution and calculated lift and drag coefficients due to pressure forces for case 1: Mach = 0.8, *Re* = 73, Incidence = 10 deg.

In the first test case, the Mach number is 0.8, the incidence is 10 deg, and the Reynolds number is 73. The Mach number contours of the computed solution are depicted in Fig. 5, where a rapid growth of the boundary layer along the upper airfoil surface is observed, and locally supersonic flow is attained only in a small pocket outside the edge of the viscous layer on the upper surface. This low Reynolds number flow provides a test of the scheme near the Stokes limit of extremely viscous flow. The computed flowfield pattern and the lift and drag values are within the same range as the results reported in the workshop.[16] A reduction of the density residuals of four orders of magnitude over 200 multigrid cycles was achieved for this case employing five meshes in the multigrid sequence as shown in Fig. 8.

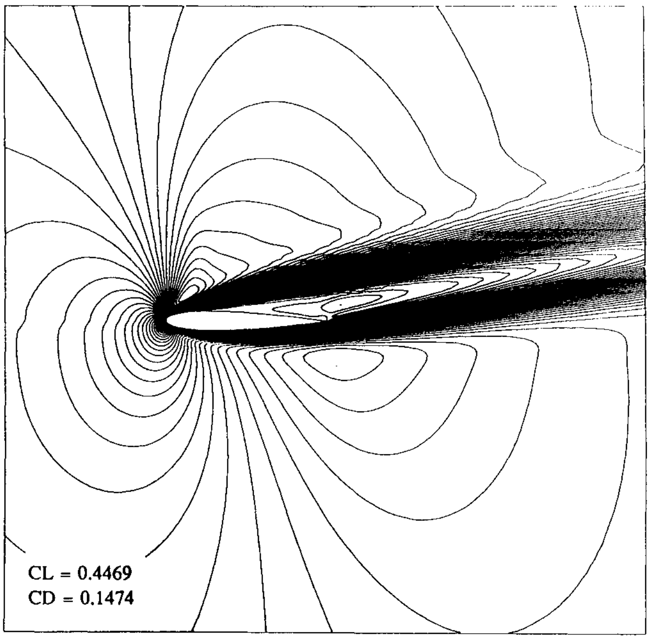

Fig. 6 Mach number contours of computed solution and calculated lift and drag coefficients due to pressure forces for case 2: Mach = 0.8, *Re* = 500, incidence = 10 deg.

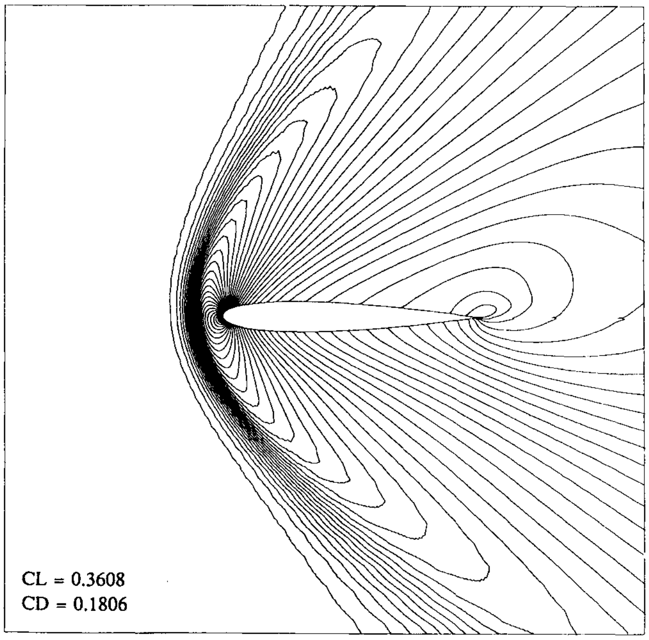

Fig. 7 Density contours of computed solution and calculated lift and drag coefficients due to pressure forces for case 3: Mach = 2.0, *Re* = 106, incidence = 10 deg.

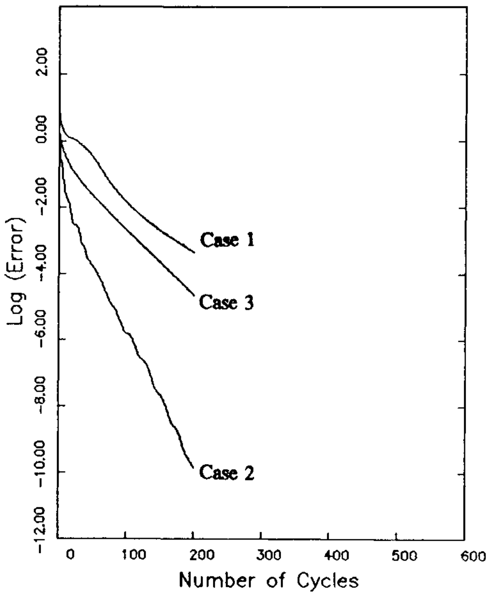

Fig. 8 Convergence rate as measured by the rms average of the density residuals vs the number of multigrid cycles on the finest mesh for the three low Reynolds number cases: case 1: Mach = 0.8, *Re* = 73, incidence = 10 deg; case 2: Mach = 0.8, *Re* = 500, incidence = 10 deg; case 3: Mach = 2.0, *Re* = 106, incidence = 10 deg.

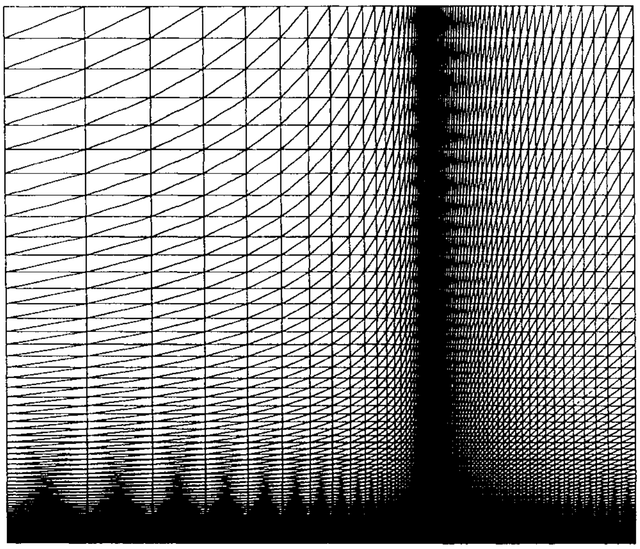

Fig. 9 Stretched triangular mesh employed for the flat-plate boundary-layer calculation; number of nodes = 5913, number of triangles = 1,1824.

In the next test case, the Mach number is 0.8, the incidence is 10 deg, and the Reynolds number is increased to 500. The Mach number contours of the computed solution are given in Fig. 6. A slower boundary-layer growth, a stronger leading-edge expansion, and an increased region of supersonic flow is observed for this higher Reynolds number case. The recompression from supersonic to subsonic flow appears to occur gradually along the upper edge of the viscous layer. Separation occurs on the top surface of the airfoil, and a large wake of low-velocity recirculating flow occurs downstream of the airfoil. Nevertheless, rapid convergence is achieved with the multigrid algorithm as shown in Fig. 8 where a reduction of 10 orders of magnitude of the density residuals is achieved in 200 cycles. The computed values of lift and drag for this case compare well with those reported in Refs. 11 and 16.

The third case consists of a supersonic low-Reynolds-number flow where the Mach number is 2, the incidence is 10 deg, and the Reynolds number is 106. This represents a standard test case, which has received wide attention in the literature and for which experimental data is available. The density contours of the computed flowfield are depicted in Fig. 7 where a strong bow shock is observed, which tends to weaken in the far field due to curvature. These computed density contours compare qualitatively with the experimental density contours and numerical solutions given in Refs. 5, 11, and 16, and the computed lift and drag values are within the same range as those reported in these references. For this case, the density residuals were reduced by five orders of magnitude over 200 multigrid cycles as shown in Fig. 8.

B. Flat-Plate Boundary Layer

An assessment of the accuracy of the scheme may be performed by examining the ability of the method to reproduce the well known, compressible, boundary-layer solution over a thermally insulated flat plate. The mesh employed for the boundary-layer calculation is shown in Fig. 9. It represents a triangulation of a stretched Cartesian grid previously employed for computing the same problem with a structured mesh solver.[17] The mesh contains 24 points ahead of the plate, 48 points along the plate in the streamwise direction, and 80 points in the normal direction. The upstream boundary is located two plate lengths ahead of the leading edge, and the upper far-field boundary is located at a distance of 2.6 plate lengths. The mesh points are clustered in the streamwise direction near the leading edge of the plate in order to better resolve the stagnation point flow in this region. The mesh point spacing at the wall is 0.0016 plate lengths resulting in elements of aspect ratio 50:1 near the trailing edge of the flat plate. The computations were performed for a Mach number of 0.8 and a Reynolds number based on the plate length of 5000. An exact analytical solution for this flow may be obtained by an

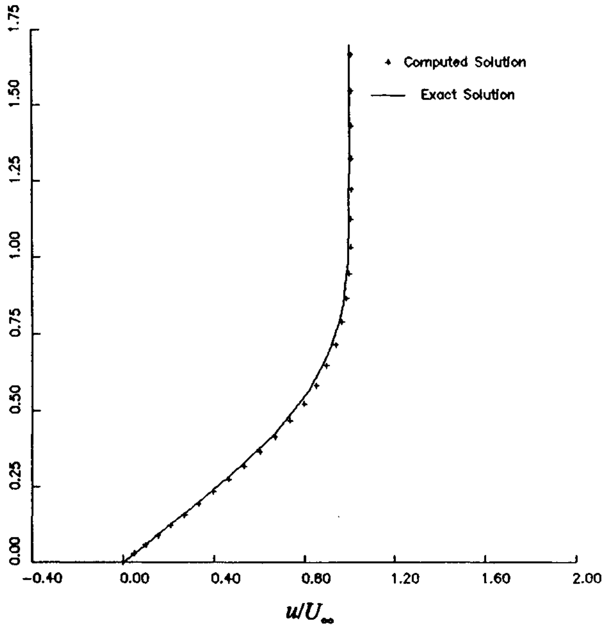

Fig. 10 Comparison of computed and exact streamwise velocity in the boundary layer at $Re_x = 3000$ in terms of similarity coordinates.

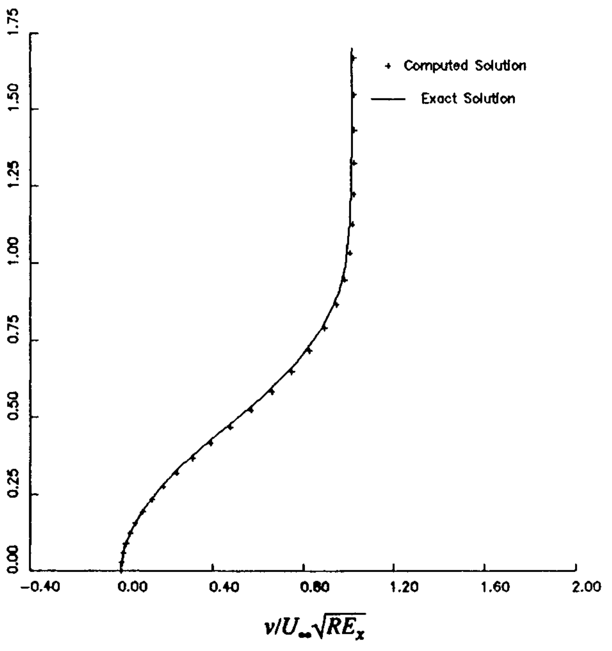

Fig. 11 Comparison of computed and exact normal velocity in the boundary layer at $Re_x = 3000$ in terms of similarity coordinates.

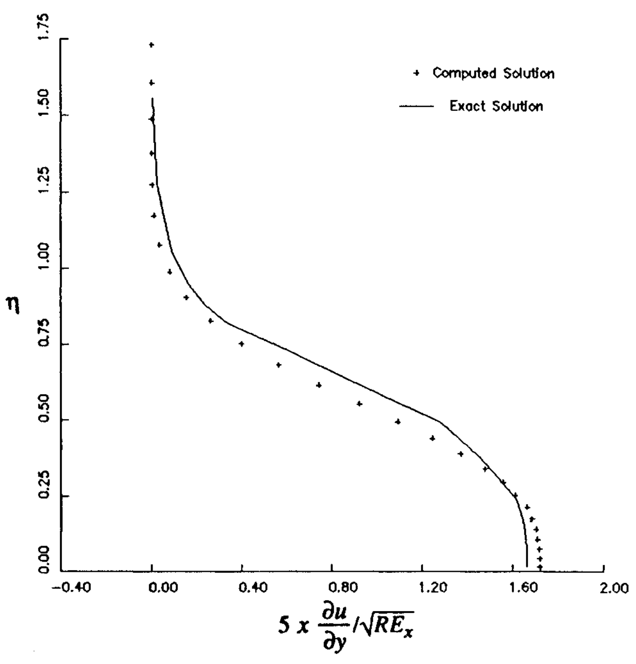

Fig. 12 Comparison of computed and exact shear stress in the boundary layer at $Re_x = 3000$ in terms of similarity coordinates.

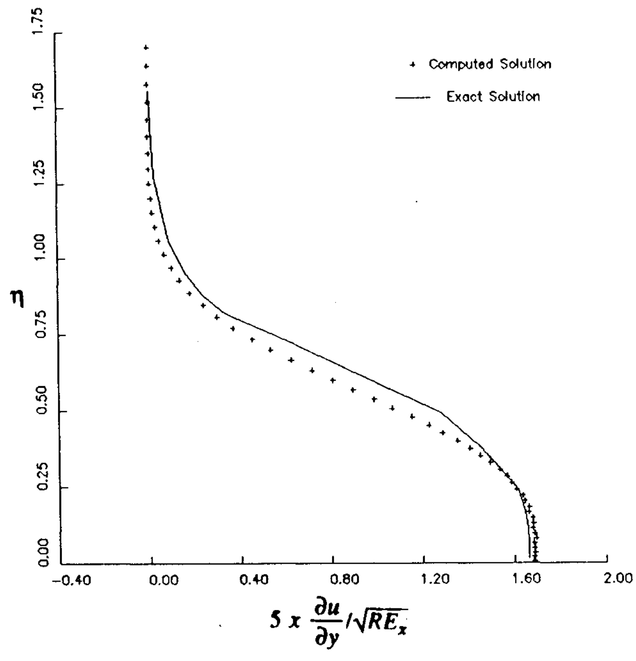

Fig. 13 Comparison of computed and exact shear stress in the boundary layer at $Re_x = 3000$ using a mesh with 160 points in the normal direction.

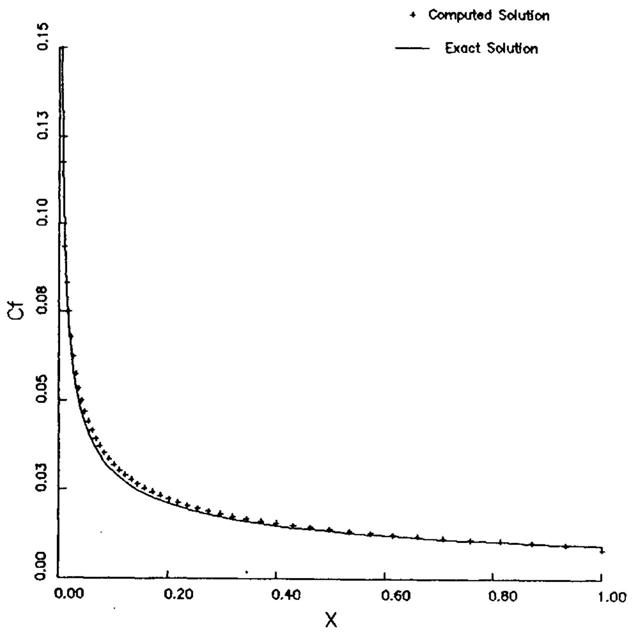

Fig. 14 Comparison of computed and exact skin friction along the plate for a Reynolds number based on the plate length of 5000, and a Mach number of 0.8.

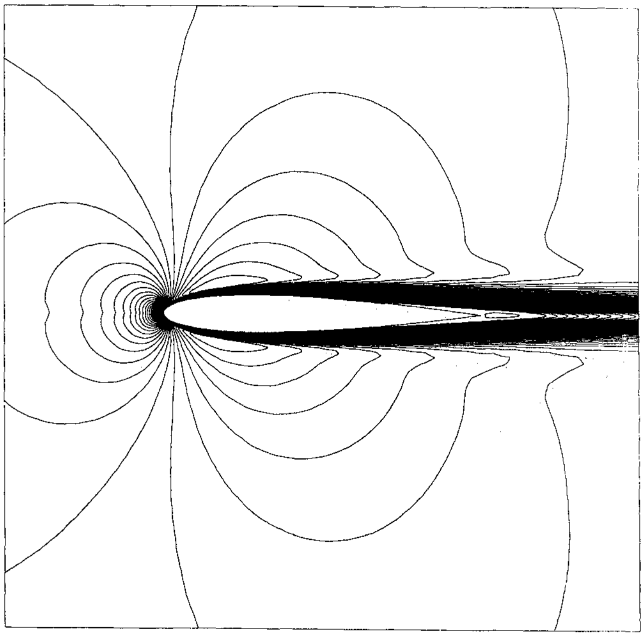

Fig. 15 Mach number contours of the computed solution for viscous flow past a NACA 0012 airfoil; Mach = 0.5, *Re* = 5000, incidence = 0 deg.

application of the Howarth-Dorodnitsyn transformation to the incompressible Blasius similarity solution.[18] The transformation consists of a rescaling of the coordinate direction normal to the plate as a function of the local density variation through the layer:

$$\bar{Y} = \int_0^\infty \frac{\rho}{\rho_\infty} \, dy \tag{43}$$

Comparison of computed and exact boundary-layer profiles at the station $x = 0.6$ for a plate of length unity where the Reynolds number based on x is 3000 are shown in Figs. 10–12. The normalized streamwise and nomal velocities, as well as the shear stress across the layer are plotted vs the similarity coordinate η, which varies from 0 to 1 through the layer, and is given by

$$\eta = \frac{\bar{Y}}{5} \sqrt{\frac{\rho_\infty U_\infty}{\mu_\infty x}} \tag{44}$$

where $\bar{Y}$ is the transformed vertical coordinate given by Eq. (43). Excellent agreement between the computed and exact profiles of streamwise and normal velocity is observed from Figs. 10 and 11. From Fig. 12, good correlation between the computed and exact shear stress across the layer is observed. The slight overprediction of the wall shear stress observed in this figure, at $\eta = 0$, could be systematically reduced by further refinement of the grid, as seen in Fig. 13, where the same case has been computed using twice the mesh resolution in the normal direction. The similarity property of the solution was also verified by examining the profiles at various different stations along the length of the plate. Good agreement was observed except for stations close to the leading edge where effects of the stagnation point flow are still present and for stations directly adjacent to the outflow boundary. The skin friction along the plate is plotted in Fig. 14, showing good agreement between computed and exact solutions except in the aforementioned regions.

For the present calculations, the κ_2 dissipation coefficient was set to zero since the flow is subcritical. The value of the κ_4 coefficient was taken as 1/256, which resulted in artificial dissipation terms, which were roughly two orders of magnitude smaller than the physical viscous terms in most regions of the boundary layer. Thus, for these values of the dissipation coefficients, the present mesh resolution, which from Figs. 10–12 can be seen to yield approximately 20 points in the layer, appears to be sufficient for accurately resolving the boundary layer. A reduction of eight orders of magnitude of the density residuals was achieved over 300 multigrid cycles for this case employing a sequence of four meshes. Similar accuracy could be obtained when the Reynolds number was raised to 50,000, and the mesh spacing at the wall was reduced to 0.0005, thus increasing the aspect ratios of the cells but retaining the same number of mesh points in the boundary layer. A somewhat slower convergence rate was observed in this case resulting in a reduction in the residuals of five orders of magnitude over 300 multigrid cycles.

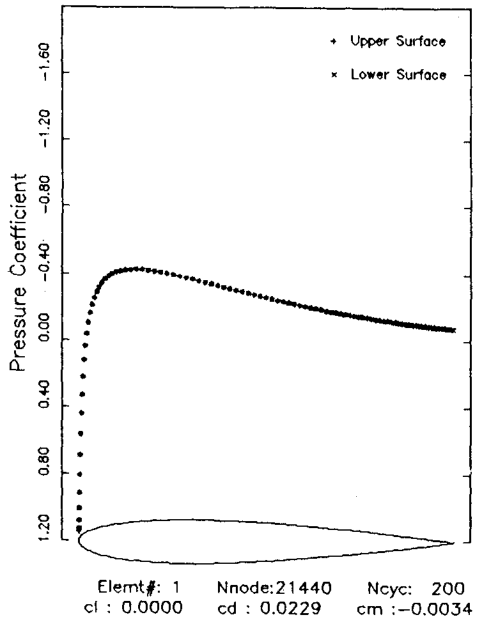

Fig. 16 Computed surface pressure distribution and calculated pressure force coefficients for flow past a NACA 0012 airfoil; Mach = 0.5, *Re* = 5000, incidence = 0 deg.

Table 1 Comparison of pressure and viscous drag coefficients and location of separation point computed by the present scheme.

NACA 0012, Mach = 0.5, Re = 5000, $\alpha = 0$ deg				
Method	Grid	CD_p	CD_v	Separation point, %
Triangle scheme $\kappa_4 = 1/256$	320 × 64	0.0229	0.0332	81.4
Triangle scheme $\kappa_4 = 1/128$	320 × 64	0.0228	0.0336	82.4
Triangle scheme $\kappa_4 = 1/64$	320 × 64	0.0225	0.0344	83.4
Cell-centered scheme from Ref. 11	320 × 64	0.0219	0.0337	81.9
Cell-vertex scheme from Ref. 13	256 × 64	0.0227	0.0327	81
Cell-centered scheme from Ref. 13	256 × 64	0.02256	0.03301	80.9
Cell-centered scheme from Ref. 13	512 × 128	0.02235	0.03299	81.4

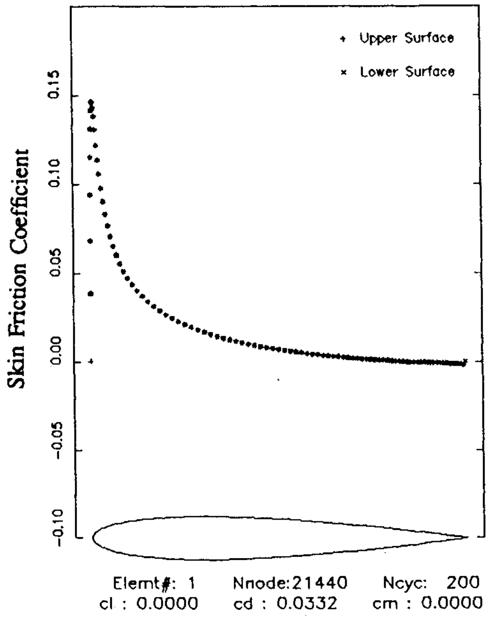

Fig. 17 Computed skin friction distribution and calculated viscous force coefficients for flow past a NACA 0012 airfoil; Mach = 0.5, Re = 5000, incidence = 0 deg.

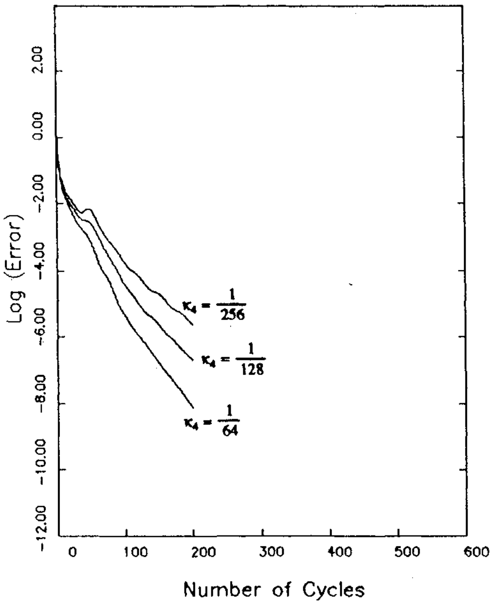

Fig. 18 Convergence rate as measured by the rms average of the density residuals vs the number of multigrid cycles on the fine mesh for various values of the artificial dissipation coefficient κ_4; Mach = 0.5, Re = 5000, incidence = 0 deg.

C. Symmetric Laminar Airfoil Case

The final test case consists of a NACA0012 airfoil at 0-deg incidence with a freestream Mach number of 0.5 and a Reynolds number of 5000. The thermally insulated wall boundary condition is applied by prescribing zero heat flux across the airfoil surface. This represents a well documented laminar test case which has been computed independently with various structured grid codes.[11-13] The Reynolds number for this case approaches the upper limit for steady laminar flow. For this case, separation occurs near the trailing edge, and a small symmetric recirculation bubble is formed in the trailing-edge and near-wake region. The mesh employed for this case is derived from a 320 × 64 structured quadrilateral C mesh with 192 points on the airfoil and 64 points in the wake. It is similar in nature to the mesh of Fig. 4, with the exception that increased stretching is applied near the airfoil surface and in the wake for better resolution of the thin viscous regions. The normal mesh spacing at the wall is 0.0002 chords resulting in cells with aspect ratios of the order of 100:1 along the airfoil. In the wake region, the element aspect ratios were limited to 100:1. Figure 15 depicts the computed Mach number contours in the flowfield, where the thin boundary-layer and wake regions are visible, and the recirculation bubble appears as a region of low Mach number flow. Plots of surface pressure and skin friction distributions are given in Figs. 16 and 17, respectively. For this subcritical case, the values of the artificial dissipation coefficients were taken as $\kappa_2 = 0.0$, and $\kappa_4 = 1/256$. This resulted in artificial dissipation terms, which were roughly two orders of magnitude smaller than the physical dissipation terms in the viscous layer regions of the flow. The classic tradeoff between accuracy and speed of convergence was observed for this case by varying the dissipation coefficient κ_4 from 1/256 to 1/64. Table 1 gives an estimate of the accuracy of the solution as measured by the computed values of pressure drag, viscous drag, and separation location vs values produced by various structured-quadrilateral-mesh Navier-Stokes solvers. The variation of the multigrid convergence rate with the change in the dissipation coefficient is illustrated in Fig. 18. The scheme is robust in that it converges efficiently over a wide range of κ_4 values, and has been found to remain stable for values as low as 1/640. Although the fastest convergence rate is achieved for a value of $\kappa_4 = 1/64$, the solution accuracy degrades slightly, the separation point having shifted from 81.4% to 83.4% chord. For all cases, convergence to engineering accuracy could be achieved in less than 100 multigrid cycles, which requires roughly 7 min of CRAY-2 CPU time. Finally, the same test case was run on a similar mesh with a normal spacing of 0.00002 chords at the wall with cell aspect ratios of the order of 1000:1 on the airfoil surface and in the wake. For a κ_4 value of 1/64, a reduction of the density residuals of 4 orders of magnitude over 200 multigrid cycles was achieved illustrating the robustness of the code in dealing with the extremely stretched elements, which are necessary for solving higher Reynolds number turbulent flows.

VI. Conclusions

A new Navier-Stokes solver for use on unstructured triangular meshes has been validated by comparing various laminar flow results about simple geometries with well established numerical and analytical solutions. The accuracy and convergence efficiency of the present scheme were found to be competitive with various well-known, structured, quadrilateral-mesh, viscous-flow solvers for laminar flow cases. The present code requires approximately 0.19×10^{-3} s/node/multigrid cycle of CPU time on a CRAY-2 supercomputer, which represents three to four times the computational effort required by equivalent structured-mesh codes. This lower computational efficiency is due in large part to the gather-scatter operations required in unstructured-mesh algorithms. In future work it will be shown how this solver can be applied to arbitrarily complex configurations which are not easily handled by structured-mesh solvers and how the efficiency and accuracy can be improved by the use of adaptive meshing techniques. The effect of truly unstructured and irregular meshes on the solution accuracy in the viscous regions will also be examined. Finally, a turbulence model for use on unstructured meshes will be sought for higher Reynolds number calculations.

Acknowledgments

The first author wishes to thank R. Radespiel of Deutsche Forschungsanstalt für Luft und Raumfahrt, Braunschweig, Federal Republic of Germany, and R. C. Swanson of the NASA Langley Research Center for their open sharing of ideas and useful suggestions. This work was performed using the computational resources of the National Aerodynamic Simulation Facility.

References

[1]Jameson, A., Baker, T. J., and Weatherill, N. P., "Calculation of Inviscid Transonic Flow over a Complete Aircraft," AIAA Paper 86-0103, Jan. 1986.

[2]Stoufflet, B., Periaux, J., Fezoui, F., and Dervieux, A., "Numerical Simulation of 3-D Hypersonic Euler Flows Around Space Vehicles Using Adapted Finite Elements," AIAA Paper 87-0560, Jan. 1987.

[3]Lohner, R., Morgan, K., Peraire, J., and Vahdati, M., "Finite Element Flux-Corrected Transport for the Euler and Navier-Stokes Equations," *International Journal for Numerical Methods in Fluids*, Vol. 7, Sept. 1987, pp. 1093–1109.

[4]Mavriplis, D. J., "Accurate Multigrid Solution of the Euler Equations on Unstructured and Adaptive Meshes," AIAA Paper 88-3707, July 1988.

[5]Bristeau, M. O., Glowinski, R., Dimoyet, B., Periaux, J., Perrier, P., and Pironneau, O., "Finite-Element Methods for the Compressible Navier-Stokes Equations," AIAA Paper 83-1890, July 1987.

[6]Morgan, K., Peraire, J., Thareja, R. R., and Stewart J. R., "An Adaptive Finite-Element Scheme for the Euler and Navier-Stokes Equations," AIAA Paper 87-1172, June 1987.

[7]Weatherill, N. P., Johnston, L. J., Peace, A. J., and Shaw, J. A., "A Method for the Solution of the Reynolds-Averaged Navier-Stokes Equations on Triangular Grids," *Proceedings of the 7th GAMM Conference on Numerical Methods in Fluids*, M. Deville, ed. Notes on Numerical Fluid Mechanics, Vol. 20, Vieweg, Braunschweig/Wiesbaden, FRG, Sept. 1987.

[8]Nakahashi N., "FDM-FEM Zonal Approach for Viscous Flow Computations Over Multiple Bodies," AIAA Paper 87-0604, Jan. 1987.

[9]Mavriplis, D. J., "Adaptive Mesh Generation for Viscous Flows Using Delaunay Triangulation," *Proceedings of the Second International Conference on Numerical Grid Generation in Computational Fluid Dynamics*, edited by S. Sengupta, J. Hauser, P. R. Eiseman, and J. F. Thompson, Pineridge Press Ltd., Swansea, UK, Dec. 1988, pp. 611–620.

[10]Mavriplis, D. J., "Multigrid Solution of the 2-D Euler Equations on Unstructured Triangular Meshes," *AIAA Journal*, Vol. 26, July 1988, pp. 824–831.

[11]Martinelli, L., "Calculations of Viscous Flows with a Multigrid Method," Ph.D, Thesis, Dept. of Mechanical and Aerospace Engineering, Princeton Univ., Princeton, NJ, Oct. 1987.

[12]Swanson, R. C., and Turkel, E., "Artificial Dissipation and Central Difference Schemes for the Euler and Navier-Stokes Equations," AIAA Paper 87-1107, June 1987.

[13]Radespiel, R., and Swanson, R. C., "An Investigation of Cell Centered and Cell Vertex Multigrid Schemes for the Navier-Stokes Equation," AIAA Paper 89-0543, Jan. 1989.

[14]Peraire, J., Vahdati, M., Morgan, K., and Zienkiewicz, O. C., "Adaptive Remeshing for Compressible Flow Computations," *Journal of Computational Physics*, Vol. 72, Oct. 1987, pp. 449–466.

[15]Mavriplis, D. J., Jameson, A., and Martinelli, L., "Multigrid Solution of the Navier-Stokes Equations on Triangular Meshes," ICASE Rept., No. 89-11, NASA CR 1817686, Feb. 1989.

[16]*Proceedings of the GAMM-Workshop on Numerical Simulation of Compressible Navier-Stokes Flows,* INRIA, Sophia-Antipolis; *Notes on Numerical Fluid Mechanics*,Vol. 18, Vieweg-Verlag, 1986.

[17]Radespiel, R., and Rossow, C., "A Cell Vertex Finite Volume Scheme for the Two-Dimensional Navier-Stokes Equations," DFVLR-IB 129-8740, DFL Internal Report, Dec. 1987

[18]Stewartson, K., "The Theory of Laminar Boundary Layers in Compressible Fluids," *Oxford Mathematical Monographs*, edited by G. Temple and I. James, Oxford Univ. Press, Cambridge, UK, 1965, pp. 33–59.